Enabling In-Situ Magnetic Interference Mitigation Algorithm Validation via a Laboratory-Generated Dataset

Matthew G. Finley[1,3,4], Allison M. Flores[2], Katherine J. Morris[1], Robert M. Broadfoot[1], Sam Hisel[1], Jason Homann[1], Chris Piker[1], Ananya Sen Gupta[2], and David M. Miles[1]

[1]Department of Physics and Astronomy, University of Iowa, Iowa City, IA, USA
[2]Department of Electrical and Computer Engineering, University of Iowa, Iowa City, IA, USA
[3]Geospace Physics Laboratory, Goddard Space Flight Center, NASA, Greenbelt, MD, USA
[4]Department of Astronomy, University of Maryland, College Park, MD, USA

Correspondence to: Matthew G. Finley (matthew.g.finley@nasa.gov)

Abstract. Magnetometer measurements are one of the critical components necessary to improve our understanding of the intricate physical processes coupling mass, momentum, and energy within near-Earth space and throughout our solar system. However, these measurements are often contaminated by stray magnetic fields from the spacecraft hosting the magnetic field sensors, and the data often requires the application of interference mitigation algorithms prior to scientific use. Rigorous numerical validation of these techniques can be challenging when they are applied to in-situ spaceflight data, as a ground truth for the local magnetic field is often unavailable. This manuscript introduces and details the generation of an open-source dataset designed to facilitate the assessment of interference mitigation techniques for magnetic field data collected during spaceflight missions. The dataset contains over 100 hours of magnetic field data comprising mixtures of near-DC trends, physically-synthesized interference, and pseudo-geophysical phenomena. These constituent source signals have been independently captured by four synchronized magnetometers sampling at high cadence and combined into 30-minute intervals of data representative of events and interference seen in historic missions. The physical location of the four magnetometers relative to the interference sources enables researchers to test their interference mitigation algorithms with various magnetometer suite configurations, and the dataset also provides a ground truth for the underlying interference signals, enabling rigorous quantification of the results of past, present, and future interference mitigation efforts.

1 Introduction

In-situ magnetometer measurements are a vital component to our search in understanding the various physical processes that couple mass, momentum, and energy throughout near-Earth space and our solar system. Magnetometers have been used to collect scientific data since the first days of humanity's exploration of space. Early missions such as Sputnik 3, Pioneer 1, and Explorer 6 all carried scientific magnetometers (Gordon & Brown, 1972). Since then, many advancements have been made to the science of triaxial spaceflight magnetometer design and implementation, enabling magnetometer suites capable of making measurements from Earth (Russell et al., 2016; Slavin et al., 2008), to Mars (Connerney et al., 2015) and the harsh radiation environment around Jupiter (Connerney et al., 2017), and even to the sun (Bale et al., 2016). Novel manufacturing processes now provide bespoke ferromagnetic fluxgate cores (Miles et al., 2019) and allow unique magnetometer topologies suitable for applications such as large constellations of nanosatellites (Greene et al., 2022).

Regardless of the improvements made to the magnetic field sensors themselves, magnetometer measurements are often contaminated by stray magnetic fields emanating from the spacecraft on which they are deployed. These interference

sources can include the battery and solar panel systems used to provide the spacecraft's power, the reaction wheels and magnetorquers used to control the spacecraft's attitude, and even the ferromagnetic materials used in the construction of the spacecraft itself (e.g., Broadfoot et al., 2022; Stolle et al., 2021; Styp-Rekowski et al., 2022). Historically, this interference has been mitigated by placing the magnetic field sensor at the end of a long boom, increasing the physical distance from the spacecraft and its associated magnetic noise sources. An additional technique for reducing the impact of the stray fields deploys multiple magnetometers at different distances along the boom; the resulting magnetic gradient between the two sensors can be fit to an ideal dipole (or multipole, if necessary) and removed from the original measurements, resulting in improved data fidelity (Ness et al., 1971).

Although this standard gradiometric approach has seen success on a wide variety of missions, it relies on long booms to achieve optimal performance. Historic missions such as MAGSAT and Voyager have seen boom lengths ranging from 6 to 13 meters (Langel et al., 1982; Miller, 1979). To reduce the cost and complexity associated with magnetic field measurements, many modern missions now utilize shorter booms. For example: Parker Solar Probe has fluxgate magnetometers deployed up to 2.7 meters from the host spacecraft (Bale et al., 2016) and CASSIOPE/Swarm-Echo operates with a 0.9-meter boom (Wallis et al., 2015). The increasingly popular CubeSat form factor may require even shorter booms, due to their significant constraints on mass, volume, and cost (Clagett et al., 2017; Miles et al., 2016). Even though these short booms reduce mission cost and technical complexity, they diminish the effectiveness of the standard gradiometric interference mitigation approach, especially in the case where the dominating interference is caused by time-varying sources such as reaction wheels. This is because the reduced separation from the spacecraft places the sensors in the interference source's near-field, meaning complex multi-pole terms can no longer be ignored. Multi-pole models can be generated to remove the time-varying interference, but these models often prove challenging to develop due to their requirement of exhaustive pre-flight characterization of all possible interference sources.

The desire for high-fidelity magnetic field data with limited boom length has recently led to the development of a variety of new approaches for the mitigation of local magnetic interference. These new techniques range from unique magnetometer configurations – such as the DAGR instrument on the Dellingr cube satellite (Clagett et al., 2017) and the NEMISIS instrument on the Lunar Gateway HERMES suite (Burt et al., 2022; Paterson et al., 2023) – to the development of new algorithms for interference identification and removal (Bowen et al., 2020; Constantinescu et al., 2020; Finley, Bowen, et al., 2023; Finley, Broadfoot, et al., 2023; Hoffmann & Moldwin, 2022; Imajo et al., 2021; Sen Gupta & Miles, 2023). The performance of the interference mitigation offered by these techniques, however, is often difficult to rigorously quantify due to the unavailability of ground-truth data from in-situ measurements.

This manuscript provides details of an open source, laboratory generated dataset intended to enable numerical analysis of existing and future interference mitigation techniques for in-situ magnetic field data. Specifically, ~10 hours of magnetic field data from four sensors in a practical configuration have been captured. The resulting dataset contains data exhibiting large near-DC trends, physically synthesized reaction wheel interference, and pseudo-geomagnetic phenomena. Further, each measurement interval of these three broad data categories were captured individually prior to their combination, effectively

providing a ground-truth for the magnetic interference and residual geophysical fields, such that the performance of interference mitigation techniques can be rigorously quantified. Additionally, the method of data combination used in this manuscript can result in >120 hours of unique field measurements suitable for testing a variety of data-intensive algorithms such as those provided by machine learning techniques.

Section 2 describes the physical apparatus used to provide magnetic stimulus and capture magnetic field data. Section 3 explains the stimulus applied to generate the three data subsets (i.e., interference, geomagnetic phenomena, and low-frequency trend), the filtering and additional steps taken to provide the combined result, and shows several examples of the combined data product. Section 4 discusses potential limitations of the dataset and avenues for future work. Finally, Section 5 summarizes and concludes this manuscript.

2 Apparatus

This section describes the physical apparatus used to produce the dataset described in this manuscript.

2.1 Magnetometers

The magnetic field sensors used for data acquisition as part of this effort are commercially available magnetoresistive vector magnetometers (VMR) produced by Twinleaf LLC. These triaxial sensors have a sensitivity of 300 pT/Hz$^{1/2}$ with a linear field range of $\pm$100,000 nT and are assumed to be calibrated out of the box. Four of these Twinleaf VMR sensors were synchronized and sampled at 200 Hz using the Twinleaf SYNC4 networking hub and associated Twinleaf I/O software. Figure 1 shows one of these magnetometers.
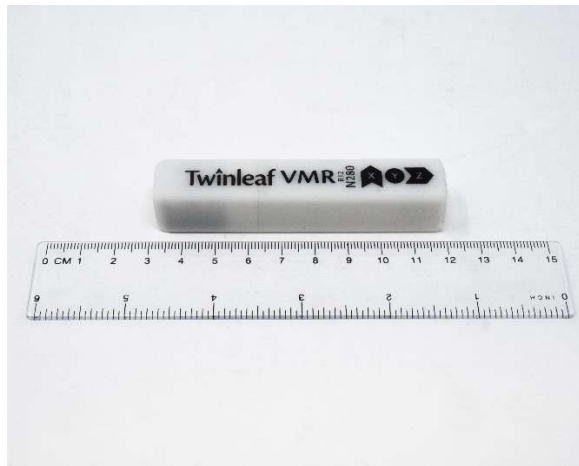
Figure 1: Twinleaf VMR magnetometer used in the generation of this dataset.

2.2 Merritt Coil

The apparatus used to simulate large near-DC magnetic fields is a 2-meter cubic 3-axis Merritt coil system (Merritt et al., 1983) shown in Figure 2. This coil system was manufactured by Serviciencia (model BM4-2000-3-A). For the collection of this dataset the coil system was connected to a Bartington PA-1 power amplifier and CU-1 control unit. The coil system has a field homogeneity of ±1% in a cube with sides of ~1-meter and can sustain a maximum steady field of ±0.9 mT. The signal generated by the coil control software is limited by the resolution of the signal generator and, per the instruction manual, has difficulty generating signals lower than 1 Hz. Signals generated at frequencies lower than ~1 Hz will exhibit significant amplitude discontinuities. However, simple filtering can be applied after data collection to mitigate the amplitude stepping in such cases. Data processing is discussed in greater detail in Section 3.2.

The coils are constructed to avoid creating conducting loops in the coil formers that could induce eddy currents, allowing for the formers to operate as single loop AC stimulus coils separately from the system. This utility allows for interesting time-varying pseudo-geomagnetic fields, such as wave packets and chirps, to be applied inside the coil via a function generator (in this case, an SRS DS360 Ultra Low Distortion Function Generator). Note that the coil system was operated in an open-loop configuration, meaning that there was no active compensation being applied to cancel the local magnetic fields. This serves to enhance the complexity of these synthetic geophysical fields by introducing fields from local magnetic phenomena.

Figure 2: Merritt coil system used to simulate various geophysical signals.

2.3 Interference Sources

105   The primary objective of this effort was to simulate magnetic interference from sources that are often difficult to characterize and remove, while maintaining an observable ground truth for numerical validation. Spacecraft are often contaminated by time-varying magnetic interference from the spinning reaction wheels used to control the vehicle's attitude. These ferromagnetic platters often rotate at rates between 2 Hz (e.g., Parker Solar Probe (Bowen et al., 2020)) and 15 Hz (e.g., Swarm-Echo (Wallis et al., 2015)). To simulate these reaction wheels two Greartisan ZGB37RG 12 V_{DC} 1000 RPM (~17 Hz)

110   electric motors were used to rotate 3D-printed plates with inset 3/8" cast iron strips. Figure 3 shows the motor with rotating plate attached.

Figure 3: Low-frequency motor and attached plate with inset cast iron strips, designed to simulate spacecraft reaction wheels.

2.4 Integrated Apparatus

115   To ensure consistency across multiple test intervals, the motors and magnetometers were rigidly mounted to a nonmagnetic plate, which was in turn mounted inside the Merritt coil. Special 3D-printed mounts were designed for both the simulated reaction wheels and magnetometers to enable proper alignment with the coil system and each other. Figure 4 provides a photograph of the integrated setup (left) and a technical drawing of the total apparatus (right). Figure 4a shows the four Twinleaf VMR magnetometers, mounted in a configuration that enables analysis of multiple magnetometer

120   configurations. For example, using only the co-linear combination of M_1 and M_2 is representative of a traditional gradiometer configuration, whereas the combination of M_2 - M_4 may be more similar to bus-mounted configurations. This enables users to test interference mitigation algorithms against various magnetometer suite topologies, which can be useful for application to missions that do not utilize a traditional co-linear gradiometer configuration (e.g., the upcoming HERMES NEMISIS magnetometers). Figure 4b shows the two simulated reaction wheels, seen in greater detail in Figure 3. The Merritt coil used

125   to generate large magnetic trends is partially shown in Figure 4c. The large rectangular object between the Twinleaf VMRs

and simulated reaction wheels is a reference magnetometer used during initial testing and setup of the coil system and is not relevant to the output dataset. The technical drawing provides measurements, in meters, referenced against the coil system. The sensors are located near the center of the coil system and should therefore be within the region of assumed homogeneity. Note that the labels $M_1 - M_4$ on the technical drawing correspond to the labels associated with each magnetometer in the output dataset.
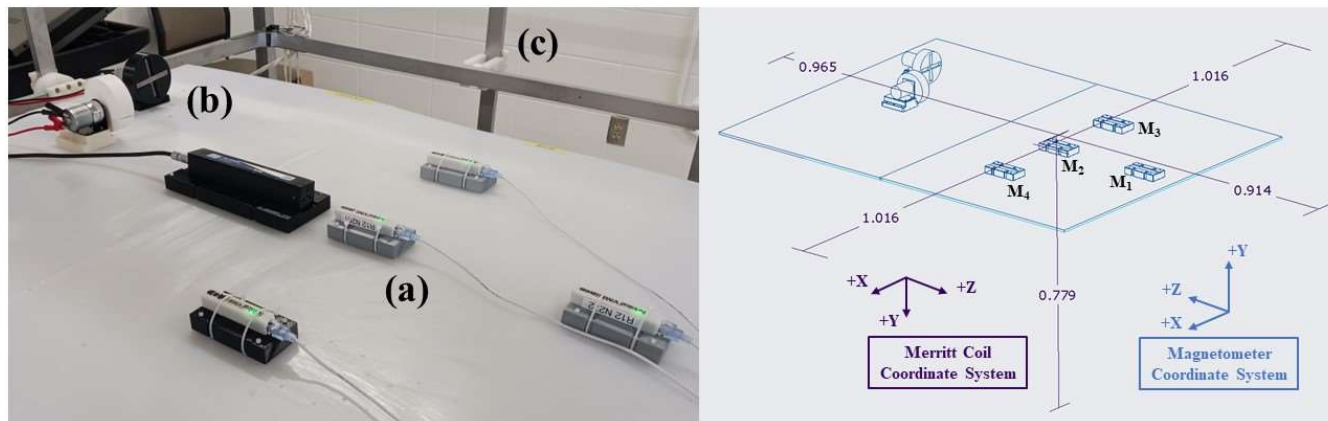

Figure 4: Experimental setup used for data collection. (Left) Photograph of experimental setup. (a) Four Twinleaf VMR magnetometers used to capture magnetic field data; (b) DC motors with attached ferromagnetic plates, used to simulate spacecraft reaction wheels; (c) Merritt coil system used to simulate geophysical fields. Note that the black rectangular object between (a) and (b) is a reference magnetometer used in this effort to ensure proper coil system operation, not for data collection. (Right) Schematic of experimental setup with measurements, in meters, referenced to the Merritt coil. Merritt coil and magnetometer coordinate systems are also illustrated.

3 Captured Data

This section provides details of the data collection and processing steps taken in the generation of this dataset. Note that all applied voltages discussed in this section are in units of V_{RMS}.

3.1 Data Acquisition

Following the deployment of the experimental setup in the coil system, various stimuli were applied to serve as proxies for the Earth's magnetic field, magnetic interference, and geophysical signals as seen by an orbiting spacecraft. Table 1 describes the different stimuli applied to the Merritt coil system (discussed in Section 2.2) used to generate the large, near-DC field serving as a proxy for Earth's magnetic field. Table 2 describes the stimuli applied to the motors (discussed in Section 2.3) used to generate physically-synthesized reaction wheel interference. Table 3 describes the stimuli, applied to the coil formers and within the coil system, used to create pseudo-geophysical wave packets and signals. The component signals corresponding to each stimulus in Tables 1 – 3 is shown, as measured by the center-most magnetometer, in detail in this manuscript's Appendix.

Table 1: Description of the stimulus applied to generate near-DC trends as a proxy for Earth's magnetic field.

Label	Stimulus Description
Near-DC Trend	
Label	Stimulus Description
Trend1	0.001 Hz sine wave with 20 V amplitude applied to coil system X-axis.
Trend2	0.003 Hz sine wave with 10 V amplitude applied to coil system Y-axis.
Trend3	0.002 Hz sine wave with 25 V amplitude applied to coil system Z-axis.
Trend4	0.001 Hz sine waves with 15 V amplitude applied to X-, Y-, Z- axes; Phase offset $\varphi = 0°, 30°, 90°$, respectively.
Trend5	0.001 Hz sine waves with 20 V amplitude applied to X-, Y-, Z- axes with no phase offsets.

Table 2: Description of the stimulus applied to generate magnetic interference as a proxy for spacecraft reaction wheels. Variable voltages induce variable speeds, simulating spacecraft maneuvers.

Label	Stimulus Description
Interference	
Label	Stimulus Description
Inter1	Motor 1 & 2 driven at 2.5 V for duration.
Inter2	Motor 1 & 2 driven at 5 V for duration.
Inter3	Motor 1 driven at 3 V for duration. Motor 2 driven at 2.5 V for duration.
Inter4	Motor 1 driven at 5 V for start. After ~15-min, adjust down to 4 V. Motor 2 driven at 4 V for duration.
Inter5	Motor 1 driven at 5 V for duration. Motor 1 driven at 5 V for start. After ~15-min, adjust up to 7.5 V, then down to 2.5 V, then back to 5 V.
Inter6	Motor 1 & 2 start at 7.5 V. After ~10-min, adjust down to 2.5 V. After ~20-min, adjust up to 6 V.
Inter7	Motor 1 driven at 7 V for duration. Motor 2 driven at 6 V for duration.
Inter8	Motor 1 driven at 3 V for start. After ~10-min, adjust up to 8 V. Motor 2 driven at 8 V for duration.

155

Table 3: Description of the stimulus applied to generate interesting magnetic phenomena as a proxy for geophysical signals.

Label	Stimulus Description
Geophysical Signals	
Label	Stimulus Description
GeoSignal1	0.75 Hz sinusoid applied to Z-axis coil former with amplitude swept from 0 V to 0.6 V_{rms} to 0 V. Stimulus applied at ~10-min and ~20-min.

GeoSignal2	0.2 V$_{rms}$ sinusoid applied to Z-axis coil former with frequency swept from 0.75 Hz to 20 Hz. Stimulus applied at ~10-min and ~20-min.
GeoSignal3	5.0 Hz sinusoid applied to Z-axis coil former with amplitude swept from 0 V to 0.6 V$_{rms}$ to 0 V. Stimulus applied at ~10-min and ~20-min.
GeoSignal4	10.0 Hz sinusoid applied to Z-axis coil former with amplitude swept from 0 V to 0.6 V$_{rms}$ to 0 V. Stimulus applied at ~10-min and ~20-min.
GeoSignal5	Vigorous ferromagnetic wrench-waving inside coil system performed by exemplary postdoc. Stimulus applied at ~5, 10, 15, 20, and 25-min.
GeoSignal6	0.1 V$_{rms}$ sinusoid applied to Z-axis coil former with frequency swept from 0.75 Hz to 20 Hz. Stimulus applied at ~8, 16, and 24-min.

3.2 Data Processing

The data exported by the Twinleaf I/O software are considered the Level 0 data product. This consists of a tab
160 separated value (i.e., *.tsv*) file, containing vector data from each of the four magnetometers, for each capture interval. The remainder of this section will discuss the data product processing pipeline necessary to convert this into a useful dataset for the validation of magnetic field interference mitigation algorithms. Note that intermediary processing steps (i.e., Level 1 and 2a) output data in a standard MATLAB v7 data format (*.mat*) for ease of readability by a variety of programs, but the final output (i.e., Level 2b) is stored in an ISTP-compliant Common Data Format file (*.cdf*).

165 ### 3.2.1 Level 1 – Filtering and Truncation

Level 1 data processing considers the measurements associated with each data category (i.e., near-DC trend, simulated interference, and pseudo-geomagnetic phenomena) independently. The Level 0 data files are first read in, parsed, and filtering steps appropriate for each type of data are applied. Note that the Level 0 data files have been converted to an easily read *.csv* format and saved as part of this dataset to enable further data calibration, combination, and processing by potential users.

170 As discussed in Section 2.2, the Merritt coil system produces amplitude discontinuities when driven at frequencies less than ~1 Hz. Therefore, a 0.1 Hz low-pass filter is applied to each instance of the near-DC data described in Table 1. This filtering reduces the impact of the amplitude steps, although some ringing is still apparent in the output. The simulated reaction wheel interference captured as described in Table 2 contains near-DC offsets from various static and time-varying local sources (including the building's elevators, nearby cars, and individuals carrying ferromagnetic objects). The sinusoidal simulated

175 interference data were brought down to a near-zero mean by subtracting a 20-second sliding average from the original data. The simulated small-scale geophysical signals described in Table 3 have no filtering applied during this stage, as spontaneous

magnetic perturbation from uncontrolled sources enhance the purpose of this data product. Finally, each interval captured is truncated to a length of 30-min, starting after 30 seconds, to avoid edge artifacts caused by the filtering process.

3.2.2 Level 2a – Data Combination

180   Level 2a data processing considers the possible combinations of Level 1 data that result in useful representations of in-situ spacecraft magnetometer measurements, enabling validation of practical interference mitigation techniques. The Level 2a data processing step results in several distinct 30-min intervals of magnetometer measurements for each broad category of data collected. Specifically, five intervals of near-DC trend, eight intervals of synthetic reaction wheel interference, and six intervals of pseudo-geomagnetic phenomena. This results in 120 hours of possible combinations when combining a single

185   interval from each category. Additional intervals of Level 2a data can be generated by utilizing multiple intervals from each category, which also serves to increase the potential data complexity.

          It should be noted that a common assumption for in-situ measurements is that geophysical magnetic fields will be identical at all scientific magnetometers onboard the spacecraft, whereas the interference measured by the sensors will fall off with distance from the body of the spacecraft. As such, when combining the data only measurements from one of four

190   magnetometers is used for the near-DC trend and geomagnetic phenomena. However, for the synthetic reaction wheel interference all four magnetometer measurements are utilized.
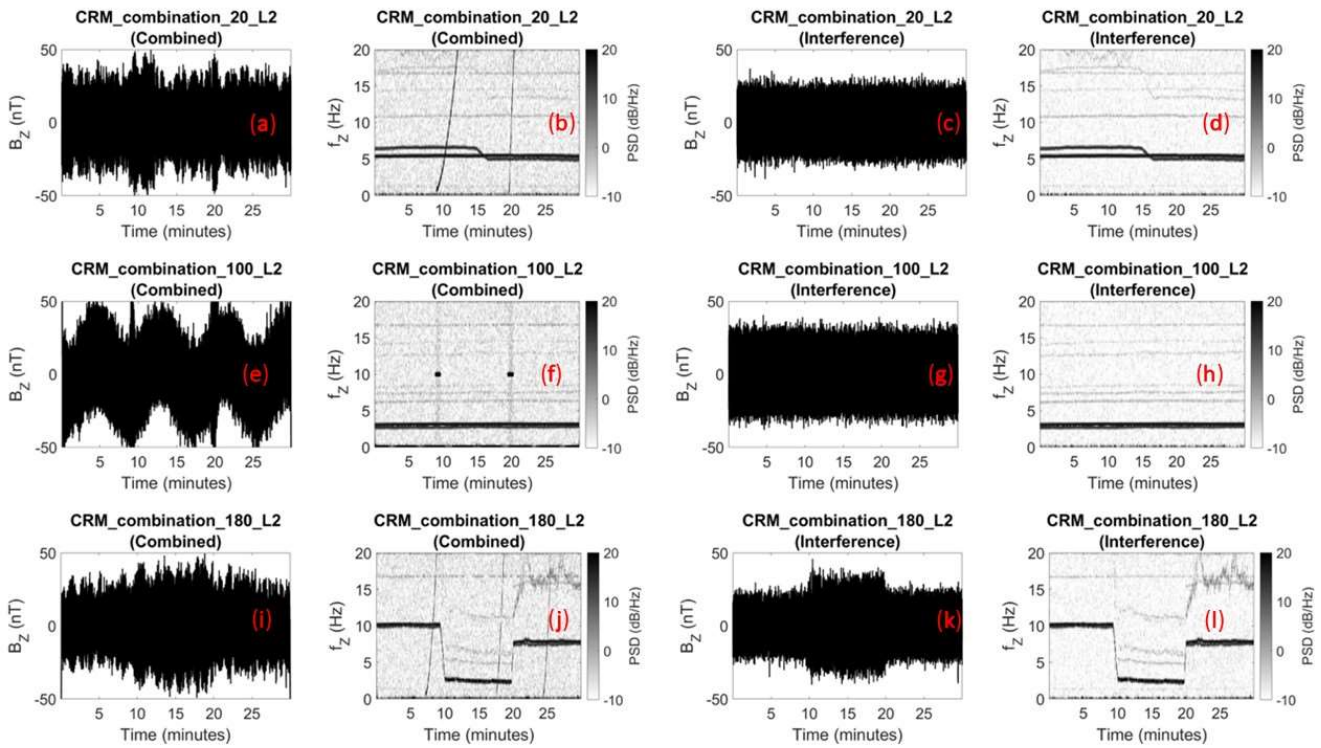
Figure 5: Sample intervals captured by M$_2$ in laboratory-generated dataset. (Column 1-2) Detrended time series and spectra associated with the combined data product; (Columns 3-4) Time series and spectra corresponding to the ground truth interference; (Row 1) Data associated with the combination of Trend2, Inter4, and GeoSignal2; (Row 2) Data associated with the combination of Trend4, Inter1, and GeoSignal4; (Row 3) Data associated with the combination of Trend3, Inter6, and GeoSignal6.

3.2.3 Level 2b – CDF Conversion

Level 2b data processing involves the transformation of the combined data generated in Level 2a into Common Data Format (*.cdf*) for enhanced accessibility and usability within the space research community. The use of .cdf files is a common practice in space research, with NASA's support ensuring widespread compatibility and longevity.

Each converted *.cdf* file contains all the essential variable information and metadata required to understand and use the data. Each file contains 16 variables corresponding to the measurements of the combined signal, interference signal, near DC-trend signal, and pseudo-geomagnetic signal for each magnetometer, separated into the sensors' x, y, and z magnetic components. Figure 5 illustrates several example data contained in the dataset. Each row in Figure 5 corresponds to a different combination of trend, pseudo-geomagnetic signal, and interference. The time series for these combinations are shown in the first column of Figure 5, with the associated spectra shown in column two. Note that the combined data have been detrended with a twenty-second moving average for ease of visualization. The interference to be identified and removed, along with its associated spectra, is shown in the third and fourth columns of Figure 5, respectively. Rows one and three illustrate combinations that have variable motor rates, which is a simulation of conditions seen during spacecraft maneuvers. The

10

210 pseudo-geomagnetic signals associated with the combinations shown in rows one and three are frequency-swept wave packets simulating geophysical phenomena such as whistler-mode waves (Teng et al., 2019). The second row of Figure 5 provides a similar example, but with fixed motor rates and an amplitude-modulated wave packet applied at a fixed frequency.

Figure 6 provides an illustration of the variables contained in a single *.cdf* file, along with some of the informative metadata describing the variable. In this case, the highlighted variable is *InterMag1*, the interference signal, measured by **M1**

215 in *CRM_combination_20_L2*. It can be seen from the descriptor text near the bottom of Figure 6 that the interference for this piece of data was generated from two motors. First, motor 1 is driven at 5V. After ~15 minutes, it was adjusted down to 4 V. Motor 2 was driven at 4 V for the total duration. The graphical output shown in Figure 6 is from the Autoplot software, a useful tool for rapidly parsing, visualizing, and analyzing *.cdf* files. Autoplot is fully compatible with the dataset presented in this manuscript, and more information about the software is available at http://www.autoplot.org.
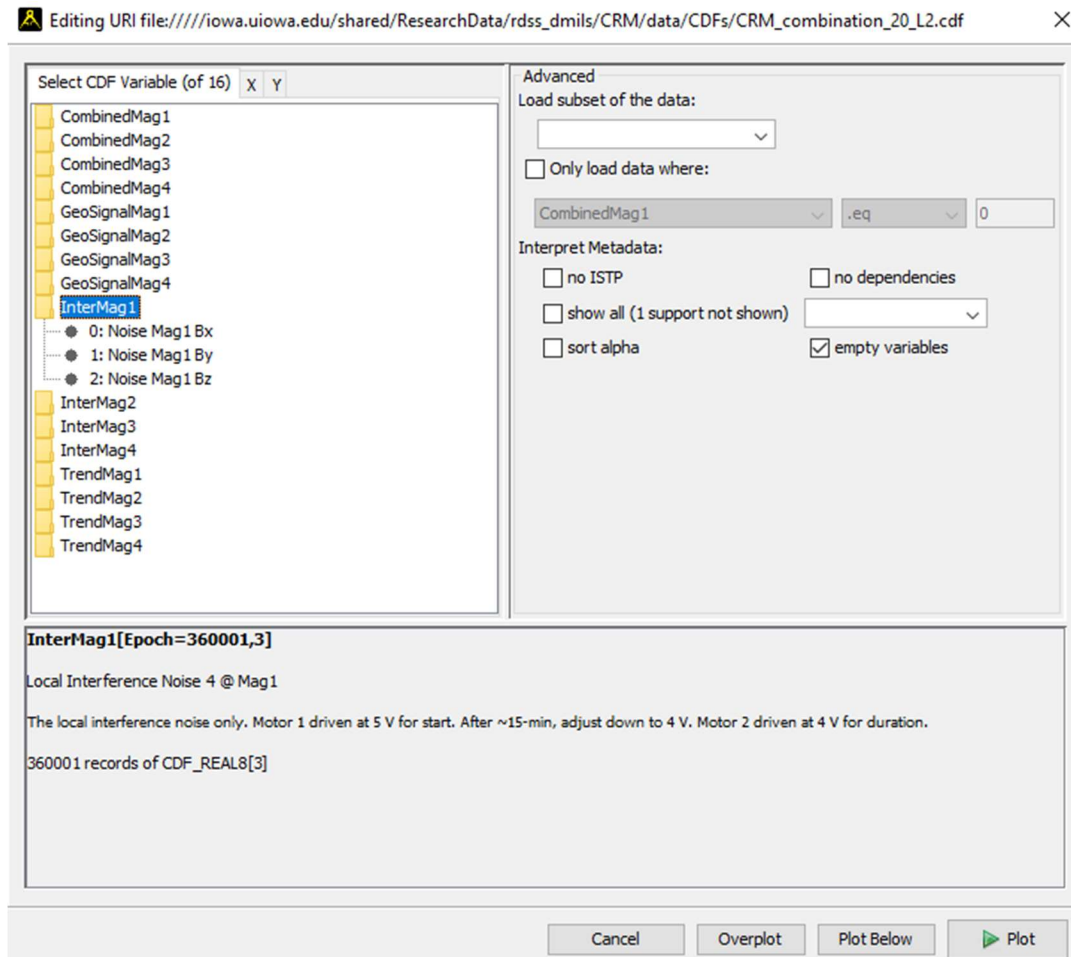
220

Figure 6: CDF variable information associated with a single data combination. In total, each CDF contains 16 variables, four for each magnetometer. Each magnetometer has measurements associated with near-DC trend, physically-synthesized interference signal, a pseudo-geophysical signal, and the combination of these constituent components. Each magnetometer measurement contains an x, y, and z component.

4 Discussion and Future Work

The primary objective of this dataset is to function as a validation tool for existing and future interference mitigation algorithms. It provides a clear distinction between interference and pseudo-geophysical signals, establishing a reliable ground truth for the validation of these algorithms. However, this section outlines several potential avenues for future work in the further development of this dataset.

Firstly, the dataset can be extended into more complex and challenging scenarios. Although the data presented in this manuscript has only combined a single interference signal with a single pseudo-geophysical signal and near-DC trend, combinations of multiple interference signals or multiple pseudo-geophysical signals can be generated that may be more difficult for some interference mitigation schemes. Additionally, the data can be time-shifted to provide more substantial spectral overlap between the pseudo-geophysical signal and interference, which is a common and challenging problem when attempting to mitigate local magnetic interference. Finally, this dataset has only provided physically synthesized proxies for a single type of local magnetic interference (i.e., reaction wheels). Although this is often a dominant source of interference on many spaceflight missions, it is not the only source of interference seen in in-situ magnetic field measurements. Spacecraft heaters, magnetic torque rods, and electrical currents from subsystems such as solar panels are commonly present in magnetometer data (Angelini et al., 2022; Stolle et al., 2021). Physical proxies for these interference sources can also be generated and added to the dataset, providing a more thorough set of example data for use in the validation of interference mitigation techniques.

It should also be noted that, although this work is intended to support interference mitigation efforts for spaceflight missions, many other fields that utilize magnetometry suffer from local magnetic interference when taking measurements. For example, many geological and archaeological surveys have begun to deploy unmanned aerial vehicles (UAVs) equipped with gradiometric magnetometer arrays to perform subsurface mapping (Zheng et al., 2021). These UAVs generate substantial local magnetic field (e.g., from their rotors, motors, and other subsystems), contaminating the measurements being taken. One common approach to mitigating these interfering local fields is to deploy the magnetometer arrays far from the UAV via a system of tethers. However, these tethers can cause additional complications when the UAV must traverse complex terrain or fly at low altitudes, and as a result more complex interference mitigation techniques must be utilized (Kaub et al., 2021). These complications are not limited to low-altitude unmanned aerial surveys, but also apply to higher-altitude manned aeromagnetic surveying (Tuck et al., 2021). One dominant source of interference seen in these various aerial magnetic surveys are the time-varying fields generated by the spinning motors onboard the aircraft (Lee et al., 2020), similar to the spinning reaction wheels used to control a spacecraft's attitude that are physically synthesized in the dataset presented in this manuscript. It can be seen that, due to the similarities between the magnetic signatures of dominant interference sources, this work can be well-suited to validate interference mitigation efforts across a wide range of fields.

5 Conclusion

In our pursuit of comprehending physical processes throughout near-Earth space and our solar system, in-situ magnetometer measurements stand as indispensable tools. Despite recent advancements in magnetometer technology, interference from spacecraft-generated magnetic fields often contaminate our scientific measurements. Historically, this interference was mitigated using a traditional gradiometric applied to two or more sensors deployed along a long boom. Many recent missions have opted for shorter booms to reduce cost and technical complexity, which also reduces the effectiveness of classical gradiometry. As a result, novel approaches for the mitigation of local magnetic interference from the spacecraft have emerged, but the quantification of their performance remains challenging due to the lack of available ground-truth data. This manuscript has presented a dataset to enable the rigorous analysis of these techniques by generating and measuring various magnetic phenomena representative of those seen by in-situ spacecraft. Specifically, ten hours of data containing near-DC trends, physically-synthesized interference, and pseudo-geophysical signals have been simultaneously captured by four magnetometers and combined to provide over 100 hours of measurements that can be used as a testbed for interference mitigation schemes. This dataset also provides a ground truth for the magnetic interference, enabling rigorous quantification of an algorithm's performance.

Appendix

This Appendix provides a more detailed view of the component signals (i.e., each near-DC trend, each physically-synthesized interference interval, and each pseudo-geomagnetic phenomena) described in Tables 1-3, as measured by the central magnetometer (M_2). Specifically, Figure 7 shows the time series associated with the near-DC trends described in Table 1. Note that the measurements shown are the axes in which the dominant signal was applied for the first three trend signals; for the last two trend signals, the Z-axis was chosen for consistency with the other plots. The spectral content associated with the near-DC trend signals is not shown, since the very low frequency of the stimuli and the substantial filtering applied to the trend signals results in uninformative spectra. Figure 8 and Figure 9, respectively, show the time series and spectral content associated with the physically-synthesized interference described in Table 2. The Z-axis is shown since it measured the highest magnitude of interference. Finally, Figure 10 and Figure 11, respectively, show the time series and spectral content associated with the pseudo-geophysical signals described in Table 3. The Z-axis is shown for these signals since it was the magnetometer axis on which the pseudo-geophysical signals were predominantly applied (i.e., for all stimuli except for *GeoSignal5* in Table 3).
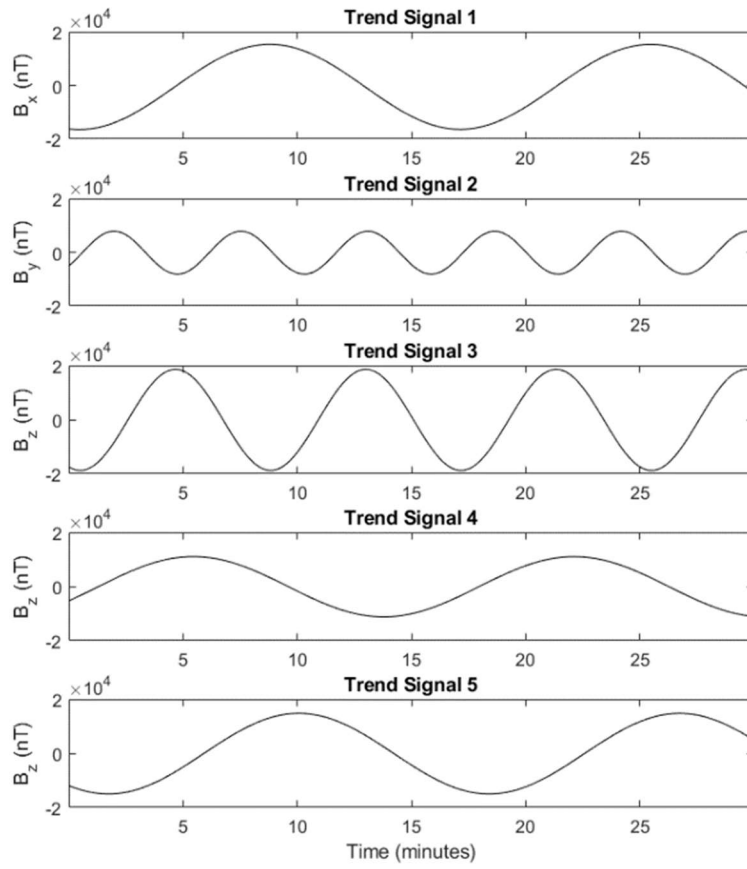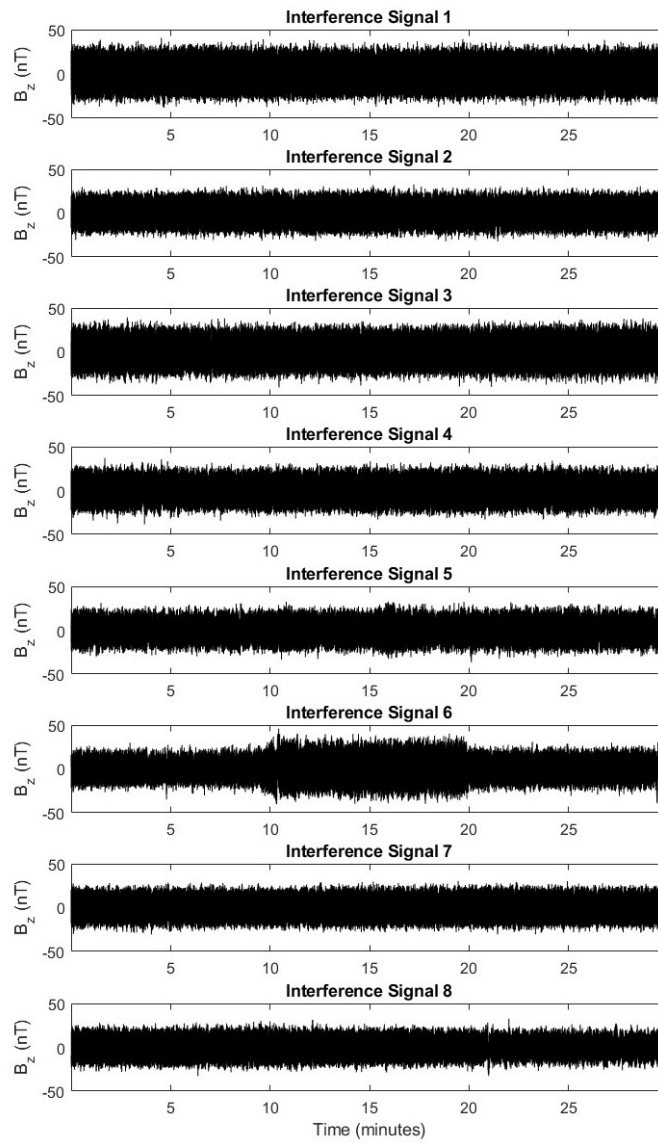
Figure 7: The component near-DC trend signals discussed in Table 1, measured by magnetometer M₂.

Figure 8: The component physically-synthesized interference signals discussed in Table 2, measured by magnetometer M₂.
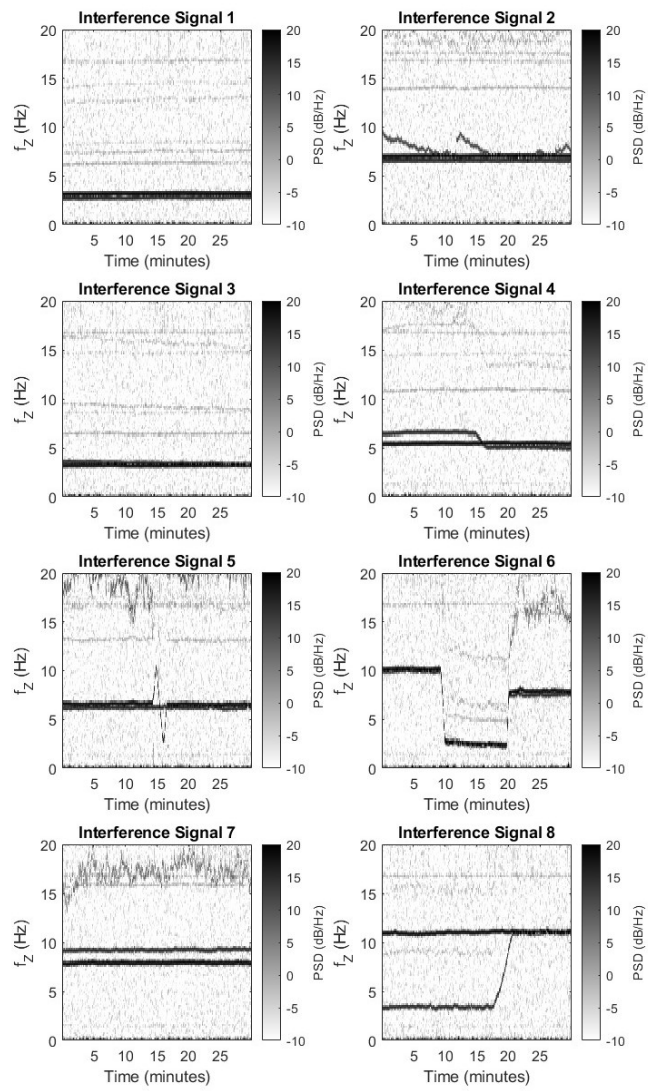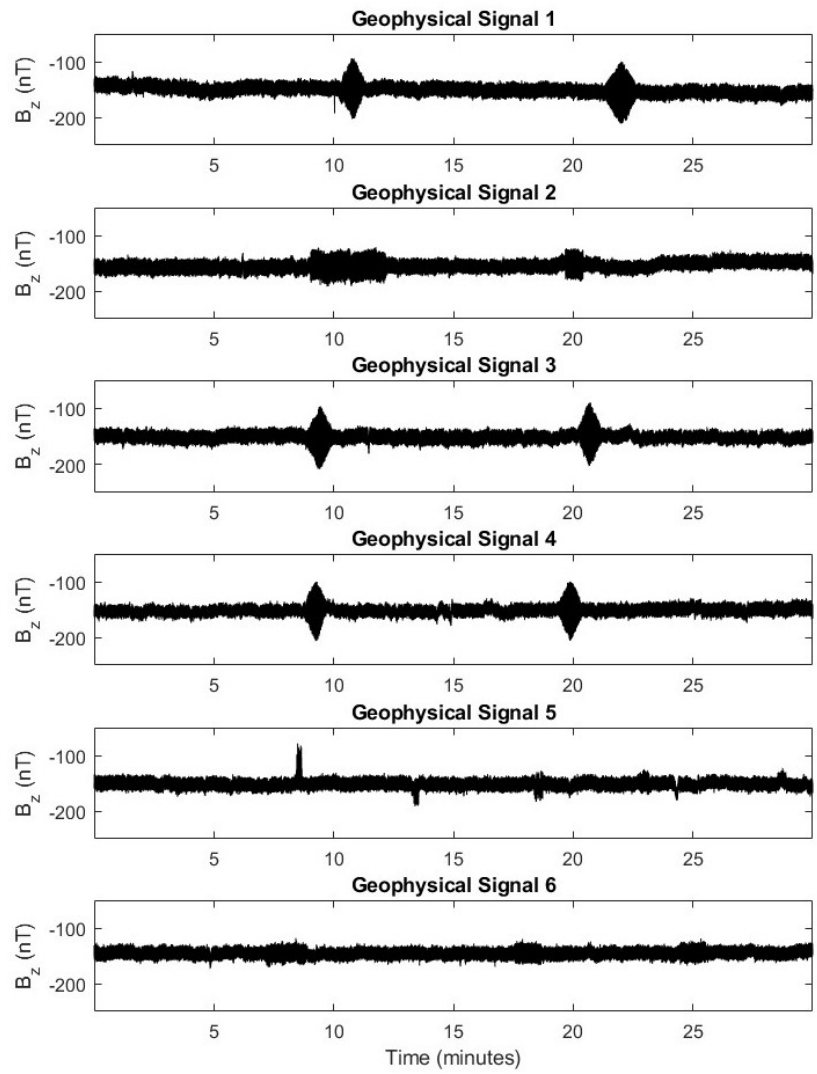
285

Figure 9: The spectra associated with the component physically-synthesized interference signals discussed in Table 2 and shown in Figure 8, measured by magnetometer M₂.

290

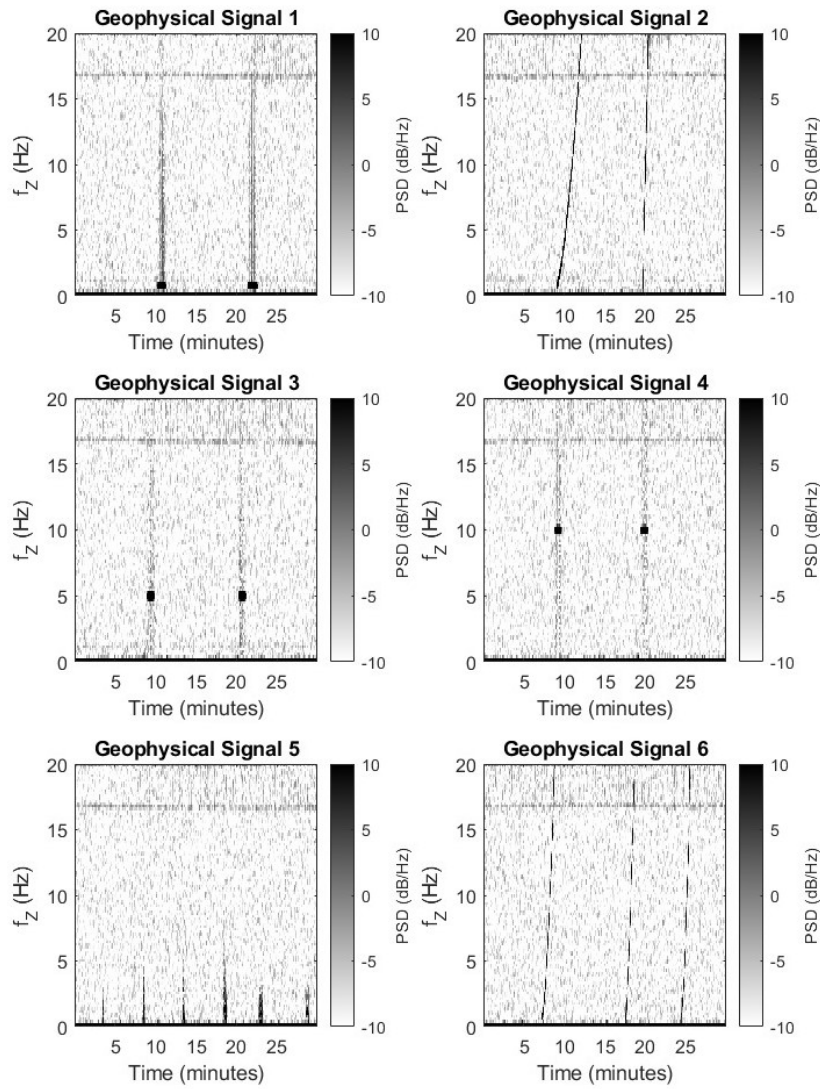**Figure 10: The component pseudo-geophysical signals discussed in Table 3, measured by magnetometer M₂.**

Figure 11: The spectra associated with the component pseudo-geophysical signals discussed in Table 3 and shown in Figure 10, measured by magnetometer M₂.

Code & Data Availability

295

The dataset presented in this manuscript is currently available at https://iowa-my.sharepoint.com/:f:/g/personal/amflores_uiowa_edu/ElhGXdssbtJFtaROKpndzuQBaX9-1nckRsluCtD0DD37aQ?e=CvjQ4H. Upon acceptance of this manuscript, the dataset, and code used to generate it, will be moved to a University of Iowa Institutional Repository for long-term storage and reuse.

Author Contribution

Finley and Miles conceptualized the project. Morris, Broadfoot, and Hisel developed the test setup. Finley, Flores, Homann, and Piker captured the data. Finley and Piker wrote the software to produce the output data product and associated metadata. Finley, Flores, and Broadfoot wrote the manuscript. All authors contributed to the proofreading of the manuscript. Miles and Sen Gupta were responsible for funding acquisition and project management.

Competing Interests

The authors declare that they have no conflict of interest.

References

315 Angelini, V., O'Brien, H., Horbury, T., & Fauchon-Jones, E. (2022). Novel magnetic cleaning techniques for Solar Orbiter magnetometer. *2022 ESA Workshop on Aerospace EMC (Aerospace EMC)*, 1–6. https://doi.org/10.23919/AerospaceEMC54301.2022.9828828

Bale, S. D., Goetz, K., Harvey, P. R., Turin, P., Bonnell, J. W., Dudok de Wit, T., Ergun, R. E., MacDowall, R. J., Pulupa, M., Andre, M., Bolton, M., Bougeret, J.-L., Bowen, T. A., Burgess, D., Cattell, C. A., Chandran, B. D. G., Chaston, C.
320 C., Chen, C. H. K., Choi, M. K., … Wygant, J. R. (2016). The FIELDS Instrument Suite for Solar Probe Plus. *Space Science Reviews*, *204*(1), 49–82. https://doi.org/10.1007/s11214-016-0244-5

Bowen, T. A., Mallet, A., Huang, J., Klein, K. G., Malaspina, D. M., Stevens, M., Bale, S. D., Bonnell, J. W., Case, A. W., Chandran, B. D. G., Chaston, C. C., Chen, C. H. K., Dudok de Wit, T., Goetz, K., Harvey, P. R., Howes, G. G., Kasper, J. C., Korreck, K. E., Larson, D., … The PSP/FIELDS and PSP/SWEAP Teams. (2020). Ion-scale
325 Electromagnetic Waves in the Inner Heliosphere. *The Astrophysical Journal Supplement Series*, *246*(2), 66. https://doi.org/10.3847/1538-4365/ab6c65

Broadfoot, R. M., Miles, D. M., Holley, W., & Howarth, A. D. (2022). In situ calibration of the Swarm-Echo magnetometers. *Geoscientific Instrumentation, Methods and Data Systems*, *11*(2), 323–333. https://doi.org/10.5194/gi-11-323-2022

Burt, J., Goans, M., Blackwood, J., & Brown, K. (2022). Heliophysics Environmental & Radiation Measurement Experiment
330 Suite (HERMES): A Small External Payload for Gateway with Big Challenges. *2022 IEEE Aerospace Conference (AERO)*, 1–11. https://doi.org/10.1109/AERO53065.2022.9843491

Clagett, C., Santos, L., Azimi, B., Cudmore, A., Marshall, J., Starin, S., Sheikh, S., Zesta, E., Paschalidis, N., Johnson, M., Kepko, L., Berry, D., Bonalsky, T., Chai, D., Colvin, M., Evans, A., Hesh, S., Jones, S., Peterson, Z., … Rodriquez, M. (2017). Dellingr: NASA Goddard Space Flight Center's First 6U Spacecraft. *Small Satellite Conference*.
335 https://digitalcommons.usu.edu/smallsat/2017/all2017/83

Connerney, J. E. P., Benn, M., Bjarno, J. B., Denver, T., Espley, J., Jorgensen, J. L., Jorgensen, P. S., Lawton, P., Malinnikova, A., Merayo, J. M., Murphy, S., Odom, J., Oliversen, R., Schnurr, R., Sheppard, D., & Smith, E. J. (2017). The Juno Magnetic Field Investigation. *Space Science Reviews*, *213*(1), 39–138. https://doi.org/10.1007/s11214-017-0334-z

Connerney, J. E. P., Espley, J., Lawton, P., Murphy, S., Odom, J., Oliversen, R., & Sheppard, D. (2015). The MAVEN Magnetic Field Investigation. *Space Science Reviews*, *195*(1), 257–291. https://doi.org/10.1007/s11214-015-0169-4

Constantinescu, O. D., Auster, H.-U., Delva, M., Hillenmaier, O., Magnes, W., & Plaschke, F. (2020). Maximum-variance gradiometer technique for removal of spacecraft-generated disturbances from magnetic field data. *Geoscientific Instrumentation, Methods and Data Systems*, *9*(2), 451–469. https://doi.org/10.5194/gi-9-451-2020

Finley, M. G., Bowen, T. A., Pulupa, M., Koval, A., & Miles, D. M. (2023). Statistical Decomposition and Machine Learning to Clean In Situ Spaceflight Magnetic Field Measurements. *Geophysical Research Letters*, *50*(13), e2023GL103626. https://doi.org/10.1029/2023GL103626

Finley, M. G., Broadfoot, R. M., Shekhar, S., & Miles, D. M. (2023). Identification and Removal of Reaction Wheel Interference From In-Situ Magnetic Field Data Using Multichannel Singular Spectrum Analysis. *Journal of Geophysical Research: Space Physics*, *128*(2), e2022JA031020. https://doi.org/10.1029/2022JA031020

Gordon, D., & Brown, R. (1972). Recent advances in fluxgate magnetometry. *IEEE Transactions on Magnetics*, *8*(1), 76–82. https://doi.org/10.1109/TMAG.1972.1067268

Greene, K., Hansen, C., Narod, B. B., Dvorsky, R., & Miles, D. M. (2022). Tesseract – a high-stability, low-noise fluxgate sensor designed for constellation applications. *Geoscientific Instrumentation, Methods and Data Systems*, *11*(2), 307–321. https://doi.org/10.5194/gi-11-307-2022

Hoffmann, A. P., & Moldwin, M. B. (2022). Separation of Spacecraft Noise From Geomagnetic Field Observations Through Density-Based Cluster Analysis and Compressive Sensing. *Journal of Geophysical Research: Space Physics*, *127*(9), e2022JA030757. https://doi.org/10.1029/2022JA030757

Imajo, S., Nosé, M., Aida, M., Matsumoto, H., Higashio, N., Tokunaga, T., & Matsuoka, A. (2021). Signal and Noise Separation From Satellite Magnetic Field Data Through Independent Component Analysis: Prospect of Magnetic Measurements Without Boom and Noise Source Information. *Journal of Geophysical Research: Space Physics*, *126*(5), e2020JA028790. https://doi.org/10.1029/2020JA028790

Kaub, L., Keller, G., Bouligand, C., & Glen, J. M. G. (2021). Magnetic Surveys With Unmanned Aerial Systems: Software for Assessing and Comparing the Accuracy of Different Sensor Systems, Suspension Designs and Compensation Methods. *Geochemistry, Geophysics, Geosystems*, *22*(7), e2021GC009745. https://doi.org/10.1029/2021GC009745

365   Langel, R., Ousley, G., Berbert, J., Murphy, J., & Settle, M. (1982). The MAGSAT mission. *Geophysical Research Letters*, *9*(4), 243–245. https://doi.org/10.1029/GL009i004p00243

Lee, H., Lee, C., Jeon, H., Son, J. J., Son, Y., & Han, S. (2020). Interference-Compensating Magnetometer Calibration With Estimated Measurement Noise Covariance for Application to Small-Sized UAVs. *IEEE Transactions on Industrial Electronics*, *67*(10), 8829–8840. https://doi.org/10.1109/TIE.2019.2950841

370   Merritt, R., Purcell, C., & Stroink, G. (1983). Uniform magnetic field produced by three, four, and five square coils. *Review of Scientific Instruments*, *54*(7), 879–882. https://doi.org/10.1063/1.1137480

Miles, D. M., Ciurzynski, M., Barona, D., Narod, B. B., Bennest, J. R., Kale, A., Lessard, M., Milling, D. K., Larson, J., & Mann, I. R. (2019). Low-noise permalloy ring cores for fluxgate magnetometers. *Geoscientific Instrumentation, Methods and Data Systems*, *8*(2), 227–240. https://doi.org/10.5194/gi-8-227-2019

375   Miles, D. M., Mann, I. R., Ciurzynski, M., Barona, D., Narod, B. B., Bennest, J. R., Pakhotin, I. P., Kale, A., Bruner, B., Nokes, C. D. A., Cupido, C., Haluza-DeLay, T., Elliott, D. G., & Milling, D. K. (2016). A miniature, low-power scientific fluxgate magnetometer: A stepping-stone to cube-satellite constellation missions. *Journal of Geophysical Research: Space Physics*, *121*(12). https://doi.org/10.1002/2016JA023147

Miller, D. C. (1979, April 1). *The Voyager magnetometer boom*. https://ntrs.nasa.gov/citations/19790013187

380   Ness, N. F., Behannon, K. W., Lepping, R. P., & Schatten, K. H. (1971). Use of two magnetometers for magnetic field measurements on a spacecraft. *Journal of Geophysical Research (1896-1977)*, *76*(16), 3564–3573. https://doi.org/10.1029/JA076i016p03564

Paterson, W. R., Gershman, D. J., Kanekal, S. G., Livi, R., Moldwin, M. B., Zesta, E., Randol, B., & Samara, M. (2023). *Heliospheric Science From Gateway With HERMES * (EGU23-8425). EGU23. Copernicus Meetings.
385   https://doi.org/10.5194/egusphere-egu23-8425

Russell, C. T., Anderson, B. J., Baumjohann, W., Bromund, K. R., Dearborn, D., Fischer, D., Le, G., Leinweber, H. K., Leneman, D., Magnes, W., Means, J. D., Moldwin, M. B., Nakamura, R., Pierce, D., Plaschke, F., Rowe, K. M., Slavin, J. A., Strangeway, R. J., Torbert, R., … Richter, I. (2016). The Magnetospheric Multiscale Magnetometers. *Space Science Reviews*, *199*(1), Article 1. https://doi.org/10.1007/s11214-014-0057-3

Sen Gupta, A., & Miles, D. (2023). Autonomous Reaction Wheel Magnetic Signature Detection Against Background Noise in Spacecraft. *IEEE Sensors Letters*, *7*(11), 1–4. https://doi.org/10.1109/LSENS.2023.3308124

Slavin, J. A., Le, G., Strangeway, R. J., Wang, Y., Boardsen, S. A., Moldwin, M. B., & Spence, H. E. (2008). Space Technology 5 multi-point measurements of near-Earth magnetic fields: Initial results. *Geophysical Research Letters*, *35*(2). https://doi.org/10.1029/2007GL031728

Stolle, C., Michaelis, I., Xiong, C., Rother, M., Usbeck, Th., Yamazaki, Y., Rauberg, J., & Styp-Rekowski, K. (2021). Observing Earth's magnetic environment with the GRACE-FO mission. *Earth, Planets and Space*, *73*(1), 51. https://doi.org/10.1186/s40623-021-01364-w

Styp-Rekowski, K., Michaelis, I., Stolle, C., Baerenzung, J., Korte, M., & Kao, O. (2022). Machine learning-based calibration of the GOCE satellite platform magnetometers. *Earth, Planets and Space*, *74*(1), 138. https://doi.org/10.1186/s40623-022-01695-2

Teng, S., Tao, X., & Li, W. (2019). Typical Characteristics of Whistler Mode Waves Categorized by Their Spectral Properties Using Van Allen Probes Observations. *Geophysical Research Letters*, *46*(7), 3607–3614. https://doi.org/10.1029/2019GL082161

Tuck, L. E., Samson, C., Laliberté, J., & Cunningham, M. (2021). Magnetic interference mapping of four types of unmanned aircraft systems intended for aeromagnetic surveying. *Geoscientific Instrumentation, Methods and Data Systems*, *10*(1), 101–112. https://doi.org/10.5194/gi-10-101-2021

Wallis, D. D., Miles, D. M., Narod, B. B., Bennest, J. R., Murphy, K. R., Mann, I. R., & Yau, A. W. (2015). The CASSIOPE/e-POP Magnetic Field Instrument (MGF). *Space Science Reviews*, *189*(1), 27–39. https://doi.org/10.1007/s11214-014-0105-z

410   Zheng, Y., Li, S., Xing, K., & Zhang, X. (2021). Unmanned Aerial Vehicles for Magnetic Surveys: A Review on Platform Selection and Interference Suppression. *Drones*, *5*(3), Article 3. https://doi.org/10.3390/drones5030093